



Polarization-independent fiber-chip grating couplers optimized by the adaptive genetic algorithm

XIAOFEI WANG, HUI YU,* QIKAI HUANG, ZHAOYANG ZHANG, ZHIYAN ZHOU, ZHILEI FU, PENGHUI XIA, YUEHAI WANG, XIAOQING JIANG, AND JIANYI YANG

Institute of Integrated Microelectronic Systems, College of Information Science and Electronic Engineering, Zhejiang University, Hangzhou 310027, China

*Corresponding author: huiyu@zju.edu.cn

Received 16 November 2020; revised 18 December 2020; accepted 18 December 2020; posted 21 December 2020 (Doc. ID 413307); published 11 January 2021

One-dimensional polarization-independent grating couplers are demonstrated with the aid of the adaptive genetic algorithm optimization. By adjusting the relative weight between the coupling efficiency and the bandwidth of the polarization-dependent loss (PDL), we control the evolution direction and customize the final performance of the device. Two specific designs are generated by giving more weight to the coupling efficiency and the PDL bandwidth, respectively. Coupling efficiencies of the first design are measured to be -7.6 dB and -7.9 dB at 1550 nm for TE and TM polarizations, respectively, while its 1.0 dB PDL bandwidth is 25.0 nm. In contrast, the second design presents higher coupling efficiencies of -7.6 dB and -7.2 dB at 1550 nm for TE and TM polarizations, respectively. However, its 1.0 dB PDL bandwidth is 22.0 nm. © 2021 Optical Society of America

<https://doi.org/10.1364/OL.413307>

Silicon photonics has been established as an excellent integration platform for a wide variety of applications, including optical interconnect [1], nonlinear photonics [2,3], sensing [4], and integrated quantum optics [5]. One advantage of silicon photonics is the high refractive index contrast, which is favorable for improving the integration density. However, it also results in big mode mismatches between silicon waveguides and single-mode fibers (SMFs). In order to effectively interface SMFs and silicon waveguides, two coupling structures are widely used, i.e., the edge coupler and the grating coupler. Each solution has its own pros and cons. Edge couplers based on inverse taper waveguides demand optical-quality facets on chip edges. They offer high coupling efficiencies and large bandwidths [6,7]. In contrast, grating couplers have advantages of relaxed fiber alignment tolerance and a simple manufacturing process. More importantly, surface normal grating couplers allow accesses to any points of a wafer, and thus enable wafer-scale testing [8–10].

Despite many merits, conventional grating couplers exhibit a strong birefringence due to the rectangular geometry of silicon waveguides, and hence support efficient coupling for only one polarization state. Several approaches have been proposed to

address this issue. One of them is to use polarization splitting grating couplers, which couple two orthogonal fiber modes to two separate waveguides [11,12]. Two sets of identical photonic integrated circuits then are used to handle the two input polarization states. Apparently, from the viewpoint to simplify the circuit, it is preferable to design a polarization-independent grating coupler that can couple different polarization states into a single waveguide with the same efficiency.

Due to technique challenges in both design and fabrication, a few polarization-independent grating couplers have been demonstrated on SOI. For example, the two-dimensional (2D) subwavelength grating (SWG) in [13] achieves a polarization-independent coupling efficiency of -6.5 dB. Its 1.0 dB polarization-dependent loss (PDL) bandwidth is 12 nm. Although the performance is acceptable, the SWG should be cladded with air on both top and bottom sides and requires a silicon layer thickness of 340 nm, which is infrequently used by the community. The other solution is based on a nonuniform one-dimensional (1D) grating whose period is formed by the mathematical intersection or union of TE and TM grating periods [14]. Its coupling efficiencies for TE and TM modes are -7.8 dB and -8.2 dB, respectively.

Compared with traditional design methods by sweeping and fine tuning a limited number of parameters, inverse design methods enabled by various mathematical optimization algorithms are capable of searching a larger parameter space, and then producing ultra-compact nanophotonic devices with excellent performances. Widely used optimization algorithms can be categorized into three groups. The first group is the gradient-based method, such as the topology optimization method [15,16] and the adjoint method [17,18]. They converge on local optima quickly by utilizing the steepest-decent optimization. However, setting up these two methods is complicated, and they require a lot of computing resources. The second group is the evolutionary method, including the genetic algorithm [19,20] and the particle swarming optimization [21,22]. These two algorithms ignore the underlying physics and have achieved remarkable successes. The third group is based on the direct binary search (DBS) algorithm [23,24].

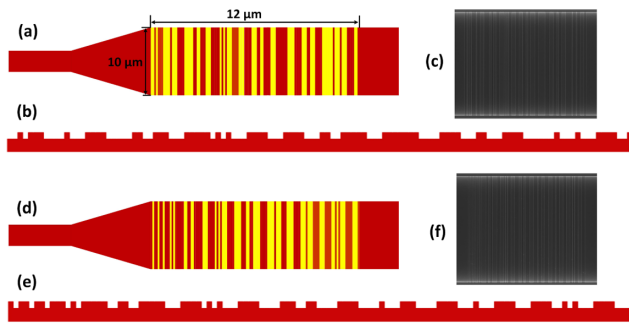


Fig. 1. Top views, cross sections, and SEM images of two optimized polarization-independent fiber grating couplers: (a)–(c) design I, (d)–(f) design II.

However, this algorithm would become less efficient when the number of design variables increases [25]. Both genetic and gradient-based optimization algorithms have been employed to design polarization-independent fiber grating couplers [26,27]. Although simulation results are promising, these works remain in the design stage owing to their low processing feasibilities. For example, designs in [26] require four or eight height levels for the silicon waveguide layer. From the viewpoint of device manufacturing, constraints imposed by practical design rule and processing flow should be taken into well account during the algorithm optimization.

In this Letter, we demonstrate 1D polarization-independent grating couplers optimized by the adaptive genetic algorithm. This algorithm is chosen here thanks to its strong global optimization ability and ease of use [28]. Many nanophotonic devices have been demonstrated successfully by utilizing this algorithm [9,19,20]. Our design utilizes typical geometrical parameters widely used by most silicon photonic integrated circuits, i.e., a 220-nm-thick Si layer and 70 nm etching depth. In addition, by adjusting the definition of the figures-of-merit (FOMs), we can manipulate the trade-off between the peak coupling efficiency and the PDL bandwidth according to different performance requirements.

Top views, cross sections, and scanning electron microscope (SEM) images of two 1D polarization-independent grating couplers are depicted in Fig. 1. Both devices are built on SOI substrate with a 220-nm-thick silicon layer and a 2-μm-thick buried oxide (BOX) layer. The grating region with a footprint of $12 \mu\text{m} \times 10 \mu\text{m}$ is discretized into 120 rectangular pixels along the longitudinal direction. The size of each pixel is $0.1 \mu\text{m} \times 10 \mu\text{m}$, and it thus can be patterned by electron-beam lithography (EBL) and inductively coupled plasma (ICP) dry etching. Yellow regions in Figs. 1(a) and 1(d) represent pixels that are shallowly etched by 70 nm, while red regions represent unetched pixels. The material state of each pixel is determined by an optimization algorithm whose goal is to achieve a polarization-independent coupling between a standard SMF28 fiber and a silicon strip waveguide. The incident angle of the fiber with respect to the surface normal is chosen to be 8 deg. Transitions from grating couplers to 220 nm × 450 nm single mode strip waveguides are implemented by 400-μm-long tapers.

The entire optimization procedure is plotted in Fig. 2(a). (i) The first generation is initialized by randomly generating 200 1D 120-bit binary sequences, which serve as 200 populations. Given that “0” and “1” denote unetched and etched pixels,

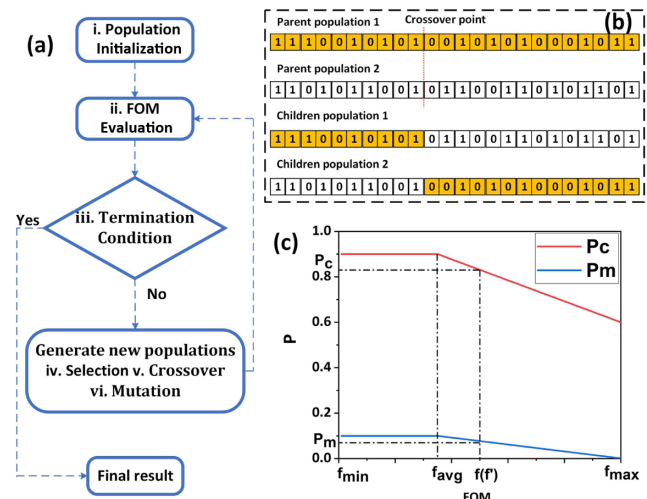


Fig. 2. (a) Genetic optimization flow chart. (b) Illustration showing the crossover process. (c) Calculated crossover probability and mutation probability as a function of the FOM.

respectively, each binary sequence corresponds to a specific grating configuration. (ii) The FOMs of each population is evaluated through the two-dimensional finite-difference time-domain (2D-FDTD) simulation. Specifically, the commercial software package FDTD solution of Lumerical is utilized to simulate coupling efficiencies of TE and TM modes in a wavelength span of 100 nm [29]. The construction of the FOM is crucial for the inverse design. After several trials, the FOM is finally defined as

$$\text{FOM} = 1 - \eta \cdot \frac{(1 - T_{\lambda=1550}^{\text{TE}} + 1 - T_{\lambda=1550}^{\text{TM}})}{2} - (1 - \eta) \cdot \sum_{i=1}^N \frac{|T_{\lambda_i}^{\text{TE}} - T_{\lambda_i}^{\text{TM}}|}{N}, \quad (1)$$

where T and λ denote the coupling efficiency and the wavelength, respectively. In Eq. (1), the performance of the polarization-independent coupler is characterized by two factors: peak coupling coefficients of TE and TM polarizations at 1550 nm, and the discrepancy between coupling coefficients of TE and TM polarizations in the wavelength range from λ_1 to λ_N . The weighting factor η controls their relative impacts on the final FOM. A large η close to 1 implies that the optimization is prone to improve peak coupling efficiencies of TE and TM modes, while a small η close to 0 implies that the consistency between coupling coefficients of TE and TM modes has a higher priority. (iii) The loop is terminated if either the maximum number of iterations is reached or the FOM does not improve for more than 30 generations. (iv) The roulette-wheel selection method is utilized to select populations for (vi) crossover and (vii) mutation according to their FOMs. Each selected population has a probability of P_c to intermix with another population at a random crossover point. This step is depicted in Fig. 2(b). The two newly generated children populations then mutate with a probability of P_m by flipping one random pixel. After that, the optimization process returns back to step (ii).

The crossover and the mutation probabilities are fixed in the conventional genetic algorithm. Therefore, populations with

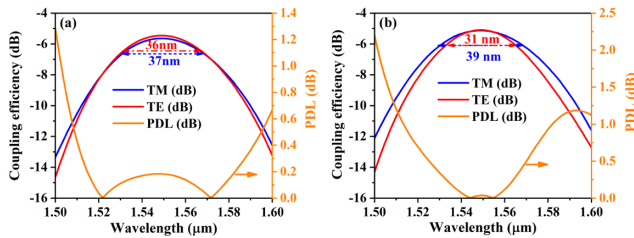


Fig. 3. Coupling efficiencies and PDLs of optimized polarization-independent grating couplers versus operation wavelength. (a) design I, (b) design II.

different FOMs share the same crossover and mutate probabilities. This strategy leads to either a slow convergence rate or a convergence to a local maximum, which is usually referred as the precocity. To solve this issue, the adaptive method is used to automatically adjust crossover and mutation probabilities according to the FOM of each population [30]. The adaptive genetic operator is constructed as

$$P_c = \begin{cases} P_{c1} - \frac{(P_{c1}-P_{c2})(f-f_{avg})}{f_{max}-f_{avg}}, & f \geq f_{avg} \\ P_{c1}, & f < f_{avg} \end{cases}, \quad (2)$$

$$P_m = \begin{cases} P_{m1} - \frac{(P_{m1}-P_{m2})(f'-f_{avg})}{f'_{max}-f'_{avg}}, & f' \geq f_{avg} \\ P_{m1}, & f' < f_{avg} \end{cases}, \quad (3)$$

where f_{max} and f_{avg} denote the largest FOM and the average FOM of all populations, respectively. f is the larger FOM of the two parent populations to be intermixed, while f' is the FOM before mutation. Values of the constants P_{c1} , P_{c2} , P_{m1} , and P_{m2} are carefully chosen as 0.9, 0.6, 0.1, and 0.001, respectively. Dependences of crossover and mutation probabilities on the FOM are shown in Fig. 2(c). If a population has a FOM below the average, it is subject to higher crossover and mutation probabilities. According to our optimization result, the adaptive genetic operator improves the coupling efficiency by 5% after the same number of iterations.

An advantage of the generic algorithm is that we can control the evolution direction by tuning corresponding parameters in Eq. (1). For example, we can put the optimization priority on either peak coupling efficiencies of the two polarizations at 1550 nm or the polarization-independent bandwidth. Corresponding parameter settings are as follows: (I) $\lambda_1 = 1500$ nm, $\lambda_N = 1600$ nm, $\eta = 0.5$, $N = 100$; (II) $\lambda_1 = 1535$ nm, $\lambda_N = 1565$ nm, $\eta = 0.8$, $N = 30$. The entire optimization process takes 260 h on a normal 4 Intel R Core™ i5-7500 CPU desktop computer. Schematic top and side views of the two generated gratings are shown in Fig. 1. Wavelength dependences of their coupling efficiencies and PDLs are presented in Fig. 3. As expected, design I in Fig. 3(a) exhibits a lower peak coupling coefficient of -5.4 dB for the two polarizations but a wider polarization-independent bandwidth of 98 nm. In contrast, the design II in Fig. 3(b) exhibits a higher peak coupling efficiency of -5.1 dB for the two polarizations. The expense is a reduced polarization-independent bandwidth of 70 nm. Here, the polarization-independent bandwidth is defined as the wavelength span within which the PDL is lower than 1.0 dB. Simulated electric field distributions of out-of-plane emissions of TE and TM modes at 1550 nm are displayed in Fig. 4 for both structures.

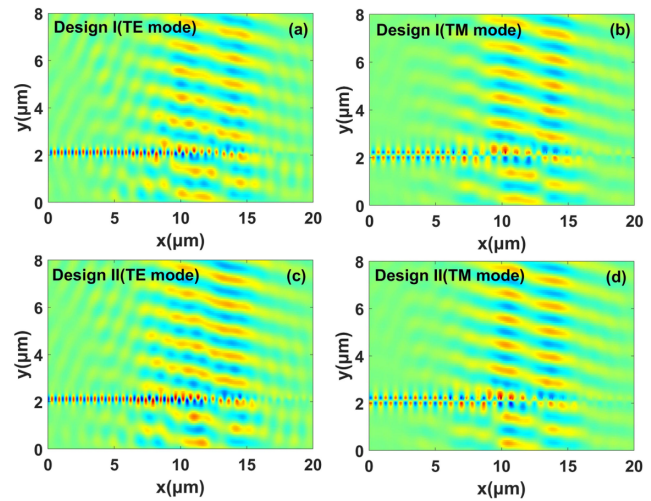


Fig. 4. Electric field distributions of out-of-plane emissions of waveguide modes at 1550 nm: (a) and (b) design I, (c) and (d) design II.

Optimized grating structures are patterned by EBL and ICP dry etching. A 2-μm-thick SiO₂ layer is deposited as the top cladding by plasma-enhanced chemical vapor deposition (PECVD). SEM images of the two fabricated grating couplers are displayed in Fig. 1.

Devices under test (DUTs) are 400-μm-long single mode strip waveguides with output ports being optimized polarization-independent grating couplers. Conventional single polarization TE or TM grating couplers with polarization extinction ratios higher than ~ 25 dB [31] are utilized as input ports. They act as optical polarizers, which convert fiber modes to desired polarization modes in Si waveguides. Coupling efficiencies of TE- and TM-type grating couplers are measured to be -4.5 dB and -5.5 dB with the aids of reference structures in the same chip.

Total fiber-to-fiber insertion losses of DUTs versus wavelength are measured with a tunable laser (Santec TSL-510) and an optical power monitor (HP 8153a). The laser output is coupled into DUTs through a polarization controller (PC). By subtracting coupling losses of input grating couplers from measured fiber-to-fiber insertion losses, we obtain coupling efficiencies of the two polarization-independent grating couplers at both polarization states. Results are shown in Fig. 5. Design I in Fig. 5(a) presents coupling efficiencies of -7.6 dB and -7.9 dB for TE and TM polarizations, respectively, at 1550 nm. Its 1.0 dB PDL bandwidth is 25.0 nm. The peak coupling efficiencies of TE and TM polarizations are -7.6 dB at 1550 nm and -7.4 dB at 1570 nm, respectively. Design II in Fig. 5(b) offers a coupling efficiencies of -7.6 dB and -7.2 dB at 1550 nm for TE and TM polarizations. Its 1.0 dB PDL bandwidth is 22.0 nm. The peak coupling efficiencies of TE and TM polarizations are -7.3 dB at 1541 nm and -7.0 dB at 1559 nm, respectively.

As expected, design II presents higher coupling coefficients than design I. Additionally, measured 1 dB bandwidths of coupling coefficients in Fig. 5 also agree well with simulation results in Fig. 3. However, measured peak coupling efficiencies of both designs are worse than the simulation results. Furthermore, measured peak wavelengths of TE and TM modes are misaligned by ~ 20 nm, and thus practical PDL bandwidths are far less than the simulation results in Fig. 3. To explain this

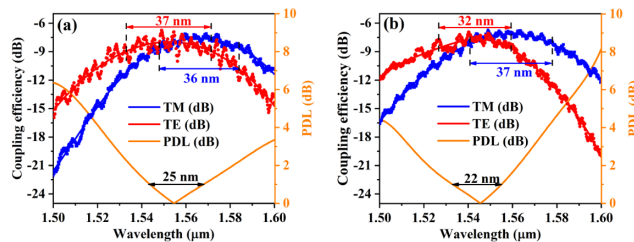


Fig. 5. Measured performances of optimized polarization-independent grating couplers: (a) design I, (b) design II.

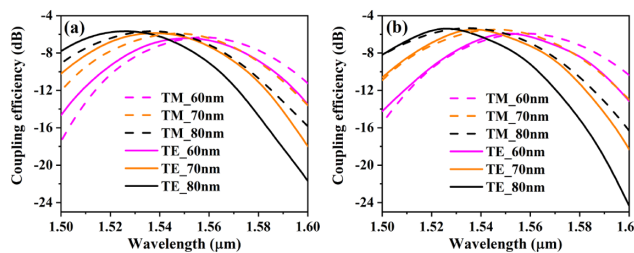


Fig. 6. Coupling efficiencies of optimized polarization-independent grating couplers versus operation wavelength by 3D-FDTD for 60 nm, 70 nm, 80 nm etching depths: (a) design I, (b) design II.

performance degradation, three-dimensional (3D)-FDTD simulations of the two designs are implemented in Fig. 6 with different etching depths. It is apparent that simulated peak coupling efficiencies reduce as the etching depth decreases. Therefore, measured low coupling efficiencies in Fig. 5 can be attributed partially to the insufficient etching depth. On the other hand, peak wavelengths of TE and TM modes are no longer well aligned in the 3D-FDTD simulation results. This point is in agreement with the measurement result. An explanation is that in our 2D-FDTD simulation, the refractive index of the silicon layer is assumed to be identical for different polarizations. To address this issue, it is suggested to use the effective index method to estimate the polarization-dependent refractive index of the silicon layer before the 2D-FDTD simulation. An alternative is to introduce a pre-offset between peak wavelengths of TE and TM modes by adjusting the objective function of the adaptive genetic algorithm.

In conclusion, the adaptive genetic algorithm is used to optimize the 1D fiber grating couplers for polarization-independent operation. The best coupling efficiency achieved is -7.6 dB and -7.2 for TE and TM polarizations at 1550 nm. We also demonstrate that by adjusting the parameter setting of the FOM, it is possible to manipulate the trade-off between the PDL bandwidth and the peak coupling coefficient. Future works include improving the optimization process so as to reduce the peak wavelength misalignment between TE and TM modes, and designing a 2D polarization-independent fiber grating coupler with relaxed requirement on the smallest feature size.

Funding. National Key Research and Development Program of China (2019YFB2203002).

Disclosures. The authors declare no conflicts of interest.

REFERENCES

- L.-W. Luo, N. Ophir, C. P. Chen, L. H. Gabrielli, C. B. Poitras, K. Bergmen, and M. Lipson, *Nat. Commun.* **5**, 3069 (2014).
- J. Leuthold, C. Koos, and W. Freude, *Nat. Photonics* **4**, 535 (2010).
- Y. Zhao, X. Ji, B. Y. Kim, P. S. Donvalka, J. K. Jang, C. Joshi, M. Yu, C. Joshi, R. R. Domeneguetti, F. A. Barbosa, P. Nussenzveig, Y. Okawachi, M. Lipson, and A. L. Gaeta, *Optica* **7**, 135 (2020).
- K. De Vos, I. Bartolozzi, E. Schacht, P. Bienstman, and R. Baets, *Opt. Express* **15**, 7610 (2007).
- A. Politis, J. C. Matthews, M. G. Thompson, and J. L. O'Brien, *IEEE J. Sel. Top. Quantum Electron.* **15**, 1673 (2009).
- J. H. Song, J. Zhang, H. Zhang, C. Li, and G. Q. Lo, *Opt. Express* **19**, 18020 (2011).
- M. Wood, P. Sun, and R. M. Reano, *Opt. Express* **20**, 164 (2012).
- D. Benedikovic, C. Alonso-Ramos, D. Pérez-Galacho, S. Guerber, V. Vakarin, G. Marcaud, X. Le Roux, E. Cassan, D. Marras-Morini, P. Cheben, F. Boeuf, C. Baudot, and L. Vivien, *Opt. Lett.* **42**, 3439 (2017).
- Y. Tong, W. Zhou, and H. K. Tsang, *Opt. Lett.* **43**, 5709 (2018).
- D. Benedikovic, C. Alonso-Ramos, S. Guerber, X. Le Roux, P. Cheben, C. Dupre, B. Szelag, D. Fowler, E. Cassan, D. Marras-Morini, C. Baudot, F. Boeuf, and L. Vivien, *Opt. Express* **27**, 26239 (2019).
- W. Bogaerts, D. Taillaert, P. Dumon, D. Van Thourhout, R. Baets, and E. Pluik, *Opt. Express* **15**, 1567 (2007).
- L. Carroll, D. Gerace, I. Cristiani, and L. C. Andreani, *Opt. Express* **22**, 14769 (2014).
- Z. Cheng and H. K. Tsang, *Opt. Lett.* **39**, 2206 (2014).
- J. H. Song, F. E. Doany, A. K. Medhin, N. Dupuis, B. G. Lee, and F. R. Libsch, *Opt. Lett.* **40**, 3941 (2015).
- J. L. P. Ruiz, A. A. Arad, L. H. Gabrielli, and A. A. Novotny, *Opt. Express* **27**, 33586 (2019).
- L. Frellesen, Y. Ding, O. Sigmund, and L. H. Frandsen, *Opt. Express* **24**, 16866 (2016).
- S. Molesky, Z. Lin, A. Y. Piggott, W. Jin, J. Vucković, and A. W. Rodriguez, *Nat. Photonics* **12**, 659 (2018).
- A. Y. Piggott, J. Lu, K. G. Lagoudakis, J. Petykiewicz, T. M. Babinec, and J. Vučković, *Nat. Photonics* **9**, 374 (2015).
- Z. Liu, X. Liu, Z. Xiao, C. Lu, H.-Q. Wang, Y. Wu, X. Hu, Y.-C. Liu, H. Zhang, and X. Zhang, *Optica* **6**, 1367 (2019).
- Z. Yu, H. Cui, and X. Sun, *Photon. Res.* **5**, B15 (2017).
- T. Watanabe, M. Ayata, U. Koch, Y. Fedoryshyn, and J. Leuthold, *J. Lightwave Technol.* **35**, 4663 (2017).
- J. C. Mak, C. Sideris, J. Jeong, A. Hajimiri, and J. K. Poon, *Opt. Lett.* **41**, 3868 (2016).
- B. Shen, P. Wang, R. Polson, and R. Menon, *Nat. Photonics* **9**, 378 (2015).
- H. Ma, J. Huang, K. Zhang, and J. Yang, *Opt. Express* **28**, 17010 (2020).
- O. Sigmund, *Struct. Multidiscip. Optim.* **43**, 589 (2011).
- X. Wen, K. Xu, and Q. Song, *Photon. Res.* **4**, 209 (2016).
- L. Su, R. Trivedi, N. V. Sapra, A. Y. Piggott, D. Vercruyse, and J. Vučković, *Opt. Express* **26**, 4023 (2018).
- M. Mitchell, *An Introduction to Genetic Algorithms* (MIT, 1998).
- <https://www.lumerical.com>.
- M. Srinivas and L. M. Patnaik, *IEEE Trans. Syst. Man Cybern.* **24**, 656 (1994).
- J. Wang, P. Chen, S. Chen, Y. Shi, and D. Dai, *Opt. Express* **22**, 12799 (2014).